Supplementary Information for

Coordinated phase separation and phase transition underlie synaptic ribbon condensate formation and plasticity

Yang Liu[1,4], Xu Wang[1,4], Tianyu Zheng[1,4], Fengfeng Niu[1,4], Ruiyi Sun[1,2], Chao Yang[2], Shun Xu[1], Zhipeng Zhao[1], Zeyu Shen[1,2], Weilin Huang[1], Xuejie Wang[2], Kai Liu[2], Shujun Cai[1,3,*], Mingjie Zhang[1,*], Zhiyi Wei[1,3,*]

[1] Shenzhen Key Laboratory of Biomolecular Assembling and Regulation, School of Life Sciences, Southern University of Science and Technology, Shenzhen, China

[2] Division of Life Science, State Key Laboratory of Molecular Neuroscience, The Hong Kong University of Science and Technology, Hong Kong, China

[3] Institute for Biological Electron Microscopy, Southern University of Science and Technology, Shenzhen, China.

[4] These authors contributed equally to this work.

[*] Corresponding author: Z.W. (weizy@sustech.edu.cn), M.Z. (zhangmj@sustech.edu.cn), and S.C. (caisj@sustech.edu.cn)

This PDF file includes:

Supplementary Figures S1 to S11

Supplementary Videos S1 to S9

Supplementary Tables S1

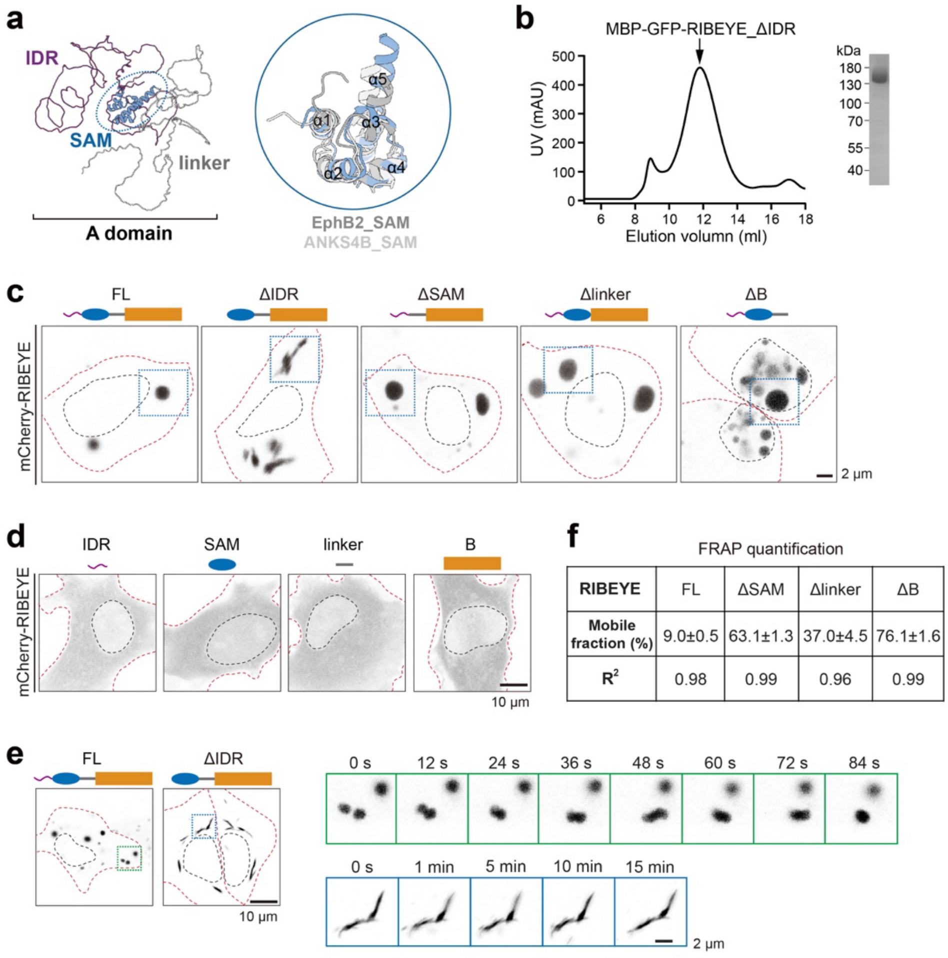

FRAP quantification

RIBEYE	FL	ΔSAM	Δlinker	ΔB
Mobile fraction (%)	9.0±0.5	63.1±1.3	37.0±4.5	76.1±1.6
R^2	0.98	0.99	0.96	0.99

Supplementary Figure S1. Structural, biochemical, and cellular characterization of RIBEYE.

a AlphaFold2-predicted structure of the A domain of RIBEYE. The predicted SAM structure of RIBEYE was aligned with the canonical SAM domains in EphB2 and ANKS4B.

b Size-exclusion chromatographic and SDS-PAGE analyses of the MBP-GFP-tagged RIBEYE_ΔIDR protein.

c Cell imaging of condensates formed by RIBEYE and its truncations overexpressed in HEK293T cells. The blue dish box indicates condensates used for FRAP analysis, shown in Fig. 1f.

d Cell imaging of HeLa cells transfected with the IDR, SAM, linker, or B fragments of RIBEYE.

e Live imaging of spherical and ribbon-like condensates formed by RIBEYE and its ΔIDR truncation overexpressed in HEK293T cells. Different dynamic behaviors of these two condensates were recorded and displayed in the right panels.

f FRAP quantification analysis of the data presented in Fig. 1g.

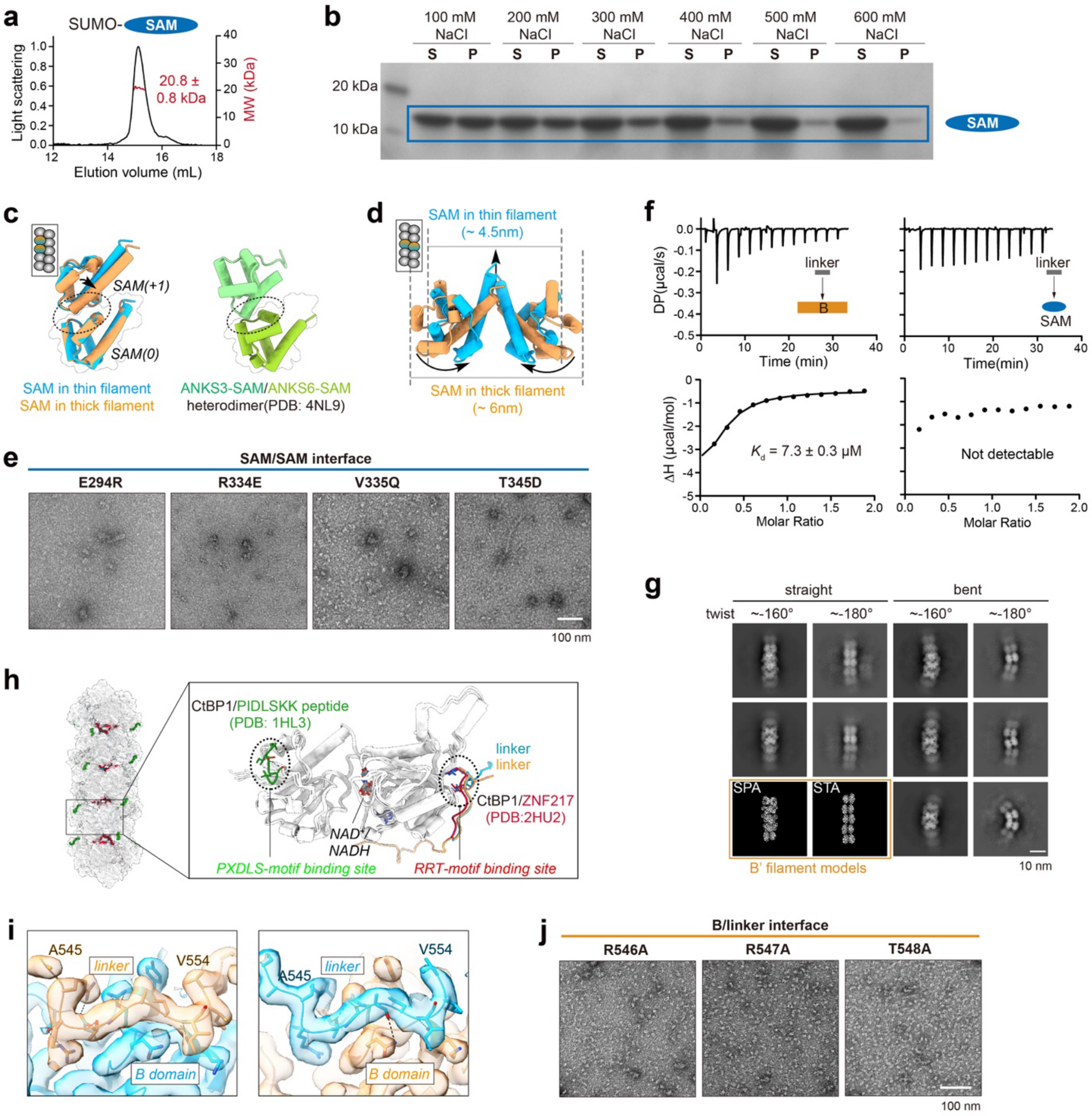

k

FRAP quantification

RIBEYE-FL	WT	E294R	R334E	V335Q	R546A	R547A	T548A
Mobile fraction (%)	7.0±0.2	12.3±2.7	36.6±6.5	16.7±1.0	26.9±2.3	36.6±2.4	16.0±1.5
R^2	0.97	0.96	0.99	0.97	0.95	0.99	0.98

Supplementary Figure S2. Biochemical and structural analyses of the SAM and B filaments.

a MALS analysis of the SUMO-tagged SAM fragment (theoretical molecular weight: 22.1 kDa). The protein concentration is 200 μM.

b Sedimentation analysis of SAM filament formation in the presence of the indicated concentration of NaCl. The SUMO tag was cleaved before sedimentation analysis. With increasing NaCl concentration, the amount of SAM filament in the pellet decreases, indicating disruption of SAM filament assembly.

c Structural comparison of thick and thin SAM filaments and ANKS3/6-SAM heterodimer. The SAM/SAM interfaces in these SAM structures are circled to indicate a similar interaction mode.

d Structural comparison of the different inter-helical interactions mediated by α5-helix between the thick and thin forms of the SAM filament. Relative conformational changes between these two forms are indicated by arrows.

e NsEM analysis showing the disruptive effects of SAM filament formation by SAM/SAM interface mutations.

f ITC-based analysis of the binding of the linker to the B and SAM domains. The protein concentration of the linker was 400 μM, while the concentration of the B and SAM domains was 40 μM.

g Cryo-EM analysis of the B' filament. The 2D classification displayed representative classes of straight and bent filaments with two distinct twist angles. As references, two atomic models of the B' filament, corresponding to these twist angles, were prepared based on the cryo-EM structure (Fig. 2g) and cryo-ET STA model (Fig. 3c), respectively.

h PXDLS- and RRT-motif binding sites on the B' filament, shown by superimposing PIDLSKK peptide (green) and ZNF217 (red) on the filament with alignment of B domains.

i Cryo-EM densities of the B/linker interface in the B' filament shown in a model-fit-map mode. The high-quality map allows unambiguous model assignment of the linkers.

j NsEM analysis showing the disruptive effects of B' filament formation by B/linker interface mutations.

k FRAP quantification analysis of the data presented in Fig. 2k.

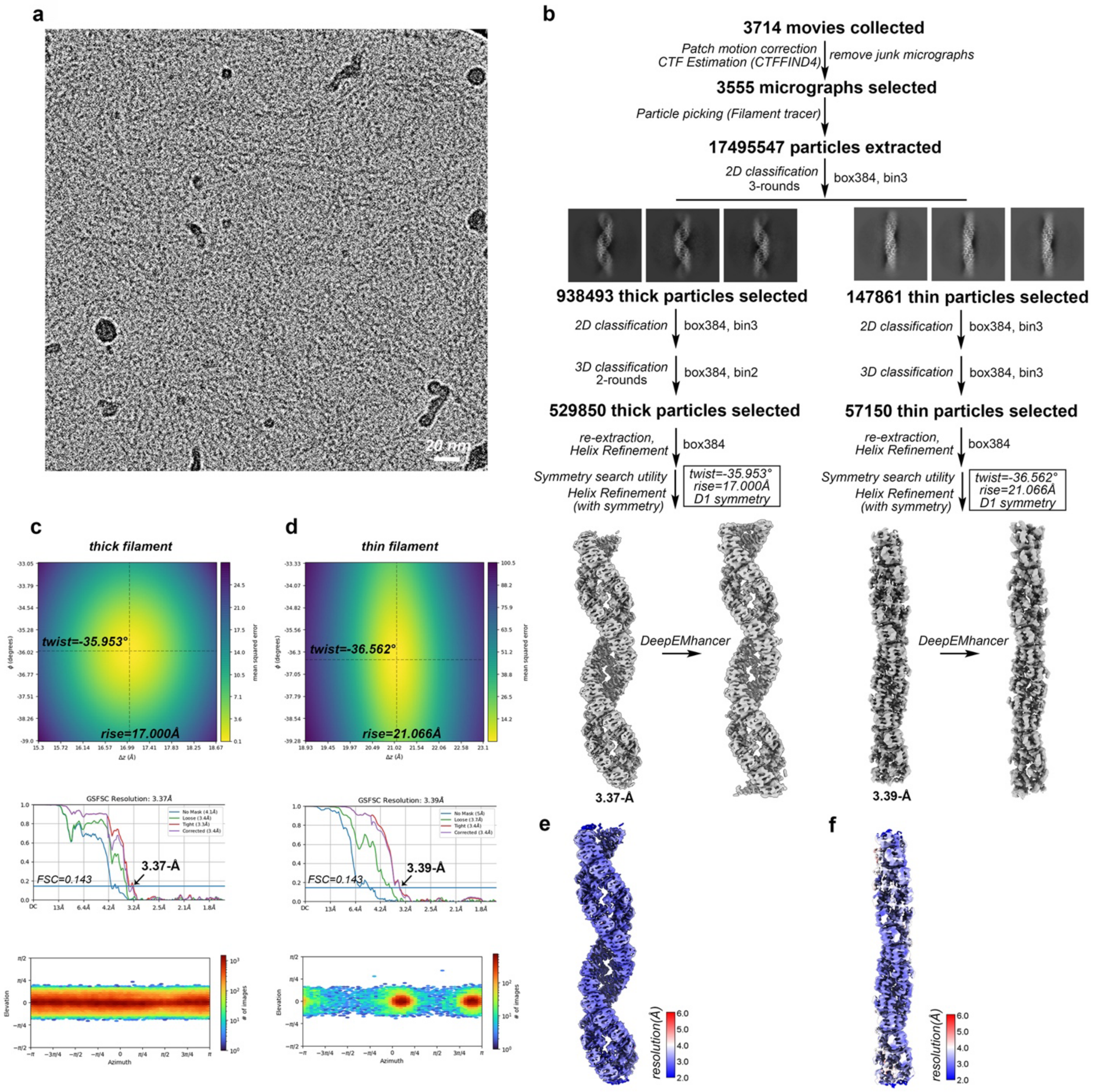

Supplementary Figure S3. Cryo-EM data processing of the SAM filament.

a A cryo-EM raw image of the SAM filament.

b Step-by-step data processing procedures to generate cryo-EM maps of the SAM filament in thick and thin forms.

c-f The estimation of helical twist and rise, the curves of gold-standard FSC to calculate the map resolution, the distribution of particle orientations, and the map local resolution estimation are represented for thick (**c, e**) and thin (**d, f**) SAM filaments, respectively.

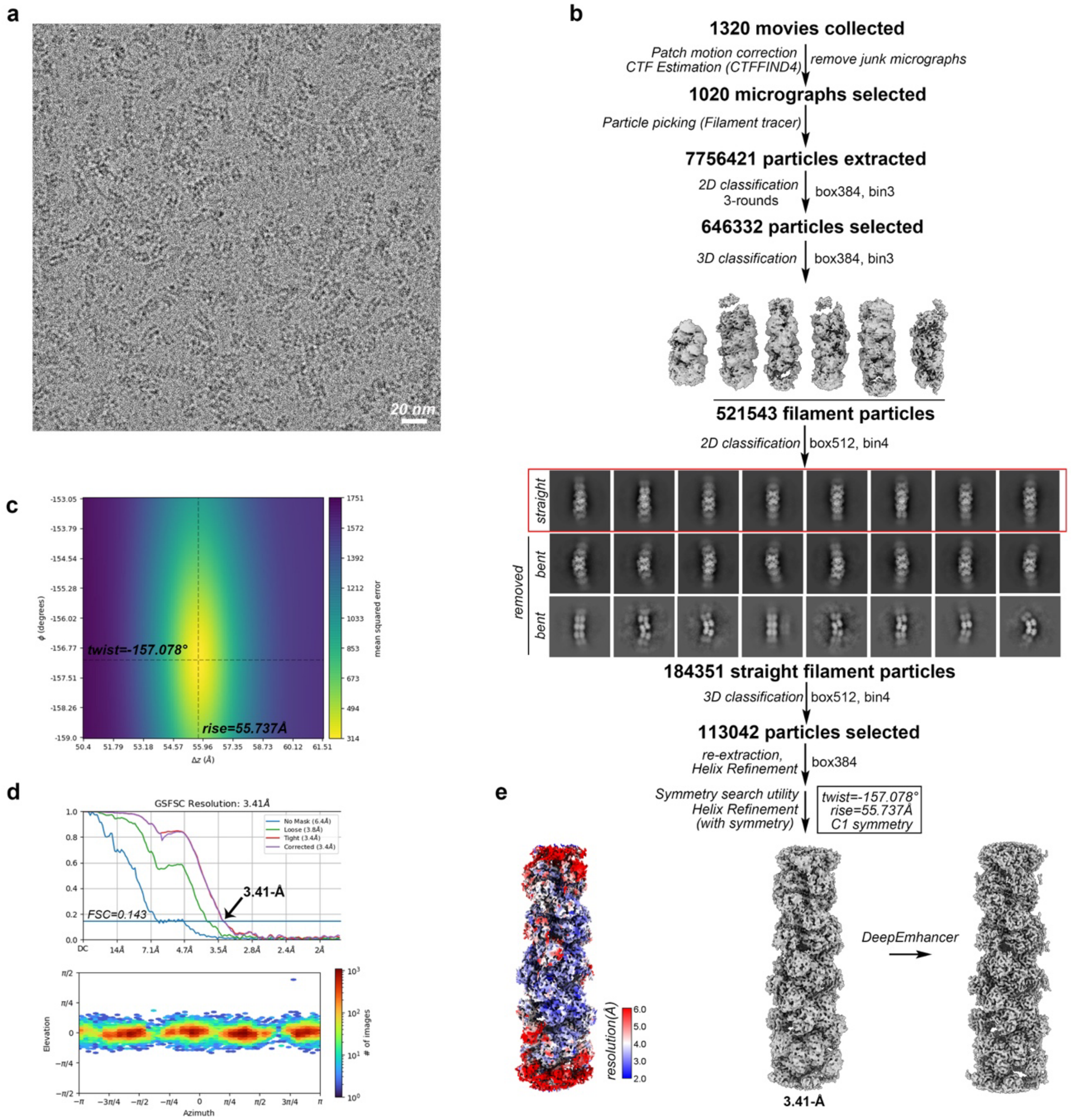

Supplementary Figure S4. Cryo-EM data processing of the B' filament.

a A cryo-EM raw image of the B' filament.

b Step-by-step data processing procedures to generate cryo-EM maps of the B' filament. The relatively straight filament particles boxed in red were selected for the following high-resolution structure determination.

c-e The estimation of helical twist and rise (**c**), the curves of gold-standard FSC to calculate the map resolution, the distribution of particle orientations (**d**), and the map local resolution estimation (**e**) are represented for the B' filament.

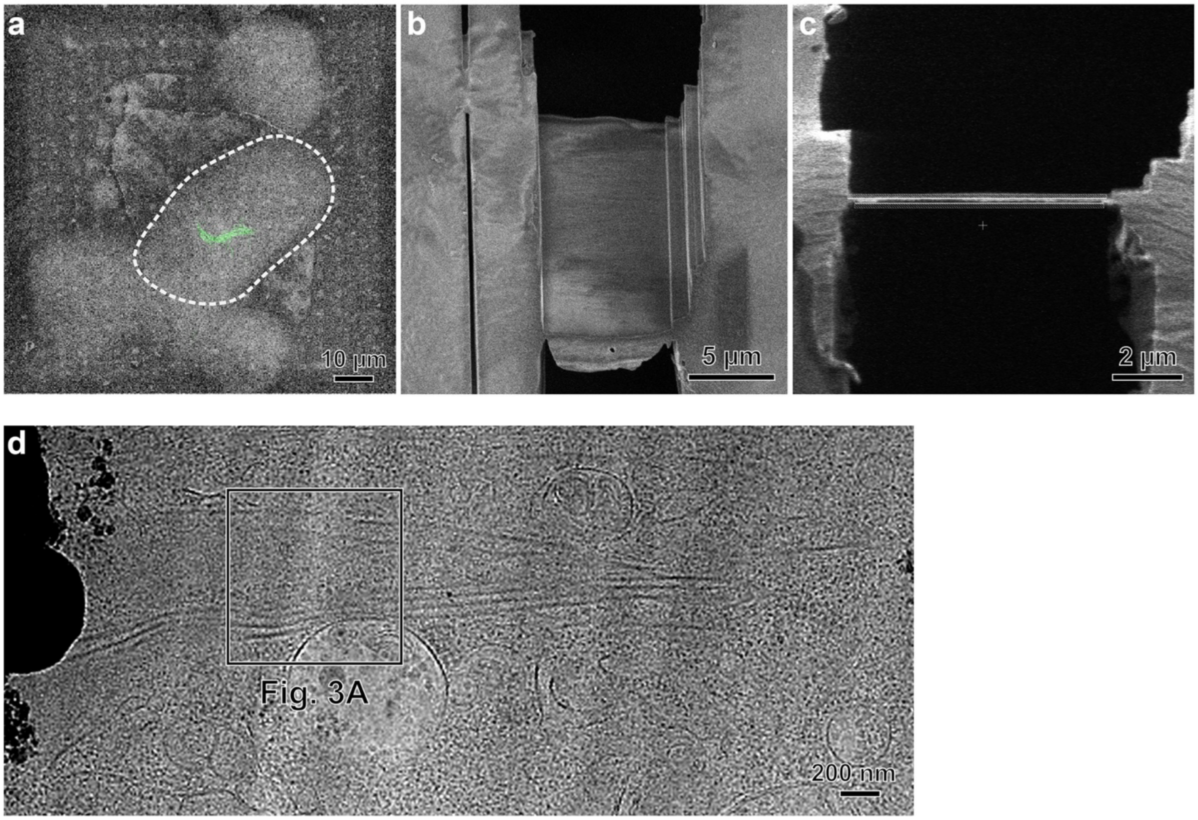

Supplementary Figure S5. Cryo-ET sample preparation of cells expressing RIBEYE_ΔIDR.

a SEM image of frozen-hydrated HeLa cells overlaid with a confocal fluorescence image of GFP-tagged RIBEYE_ΔIDR. The GFP signal was used to guide subsequent cryo-FIB milling. The dashed line represents the boundary of a cell.

b, c SEM view and ion-beam view, respectively, of a ~150-nm-thick cryo-FIB-milled lamella.

d Low-magnification cryo-EM projection image of a cryolamella. A cryo-ET tilt series was collected at the boxed region, with the corresponding reconstructed tomogram shown in Fig. 3a.

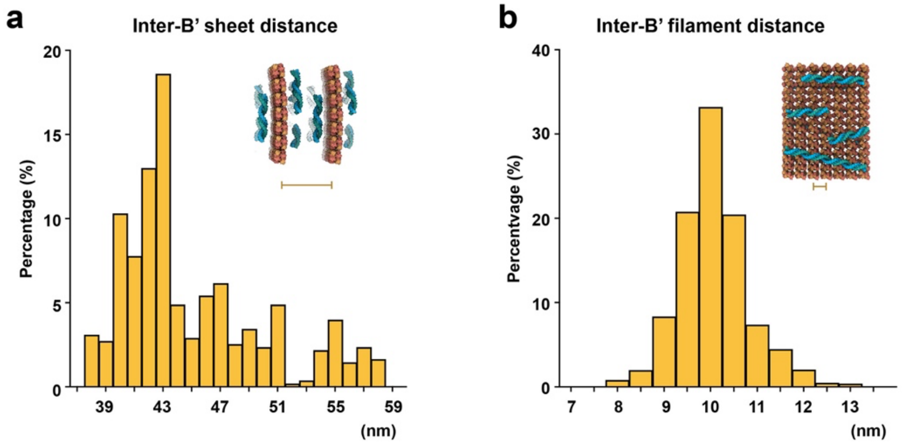

Supplementary Figure S6. Histogram-based analysis of inter-sheet and inter-filament distances in the ribbon-like condensates formed by RIBEYE_ΔIDR.

a Quantification of inter-B’ sheet distances. Distances were measured as the center-to-center spacing between adjacent B’ sheets throughout the tomogram.

b Quantification of inter-B’ filament distances. Distances were measured as the center-to-center spacing between adjacent B’ filaments throughout the tomogram.

Data are generated based on cryotomographic slices of GFP-tagged RIBEYE_ΔIDR expressed in HeLa cells.

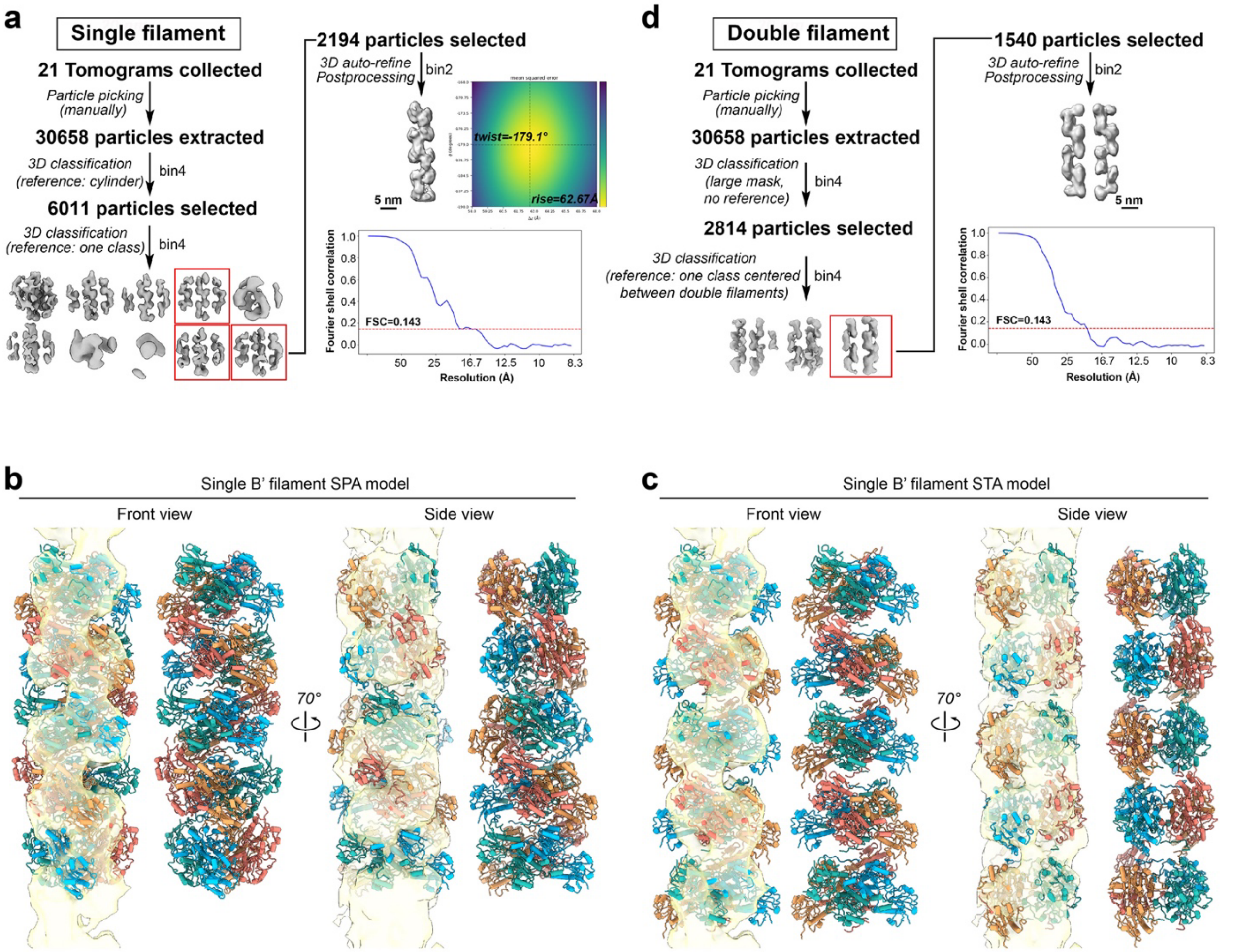

Supplementary Figure S7. STA workflow and model fitting for single and double B' filaments.

a STA workflow for single B' filaments. The workflow began with a featureless cylindrical reference. A class average or refined map that resembled the single-particle cryo-EM structure of the B′ filament was then selected as the reference for subsequent iterative classification and refinement. Final refinement was performed with binned (2×) data, as unbinned data did not yield further improvements. The helical twist and rise of the STA density were estimated by using Symmetry Search Utility in CryoSPARC. The curve of gold-standard FSC to calculate the map resolution was indicated.

b, c Superimposition of B' filament models with the STA density map of the single filament. The single B' filament models derived from SPA (**b**) and STA (**c**) were each fit into the STA density map of the single filament. For comparison, their top tetramers were aligned in the same orientation within the STA density map.

d STA workflow for double B' filaments. No reference was used in the first round of 3D classification. A large mask encompassing three filaments was applied during the initial rounds of 3D classification. Then the densities corresponding to two adjacent B' filaments from one 3D class were centered within the box and used for further classification and refinement. Final refinement was performed with binned (2×) data, as unbinned data did not yield further improvements. The curve of gold-standard FSC to calculate the map resolution was indicated.

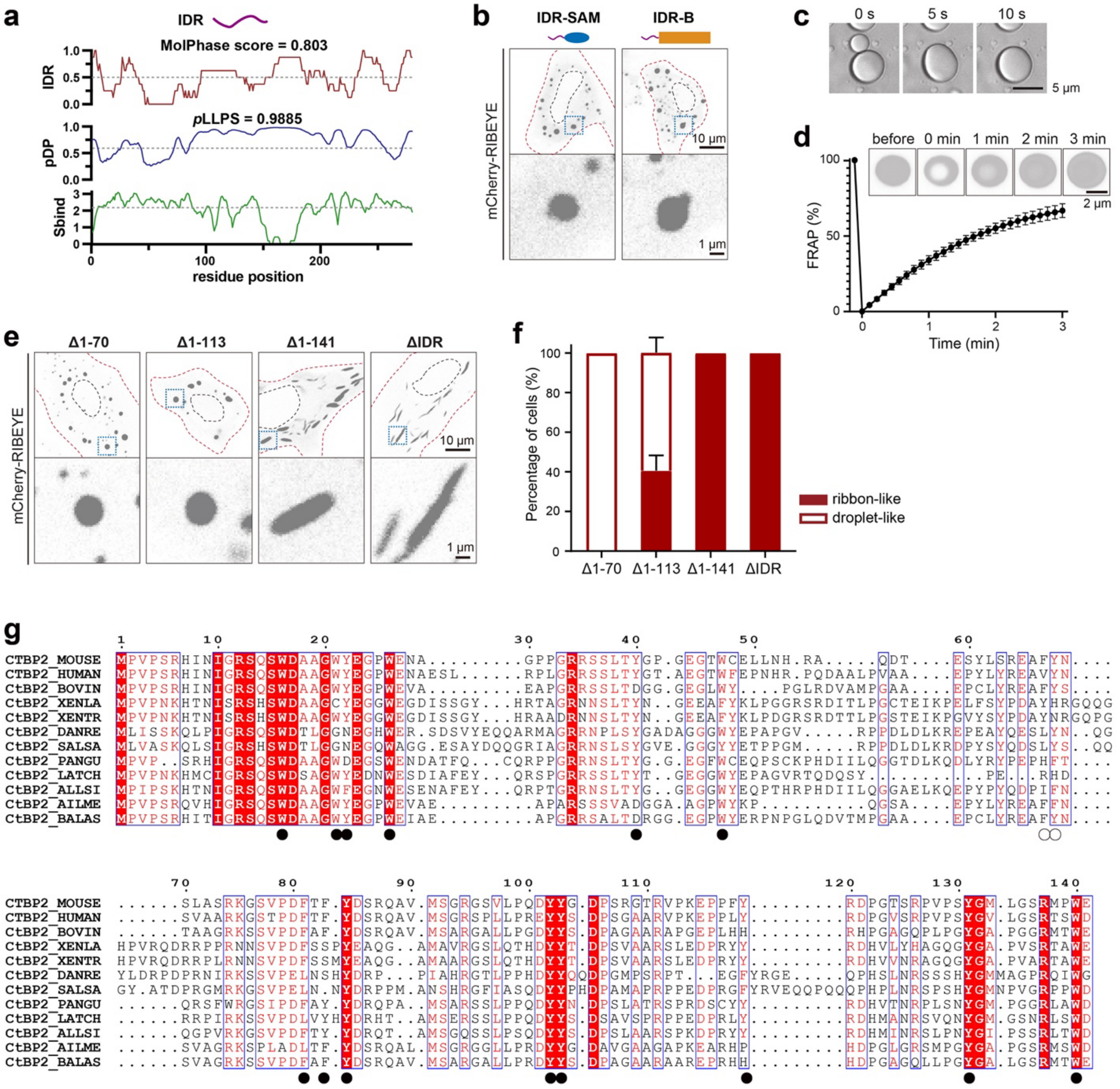

Supplementary Figure S8. Analyses of the LLPS-promotion capability of the IDR in RIBEYE.

a Sequence-based prediction of the phase separation probability in RIBEYE_IDR. The residue-based IDR score is calculated using MolPhase (https://molphase.sbs.ntu.edu.sg). The residue-based droplet-promoting probabilities (pDP) and cellular context-dependence (Sbind) are calculated using FuzDrop (https://fuzdrop.bio.unipd.it/).

b HeLa cell imaging of condensates formed by IDR-SAM and IDR-B, showing that the IDR promotes the transition of both the SAM and B domains from a diffuse cytosolic distribution to droplet-like condensates.

c Representative images of a fusion event of IDR droplets in the presence of 3% (w/v) PEG 8000. The protein concentration is 40 µM.

d FRAP analysis of condensates formed by RIBEYE_IDR in the presence of 3% (w/v) PEG 8000. The protein concentration is 40 µM. n = 8 condensates. The estimate of variation is indicated by the s.e.m..

e HeLa cell imaging of condensates formed by RIBEYE with different N-terminal truncations.

f Quantification of condensate morphology in cells shown in panel **e**. n = 3 repeats, in each repeat 20-40 cells are quantified. The estimate of variation is indicated by the s.d..

g Alignment of the IDR sequences from different species, including human, bovine, mouse, *Danio rerio*, *Xeenopus laevis*, *Xenopus tropicalis, Latimeria chalumnae, Alligator sinensis, Salmo salar, Balaenoptera acutorostrata, Pantherophis guttatus*, and *Ailuropoda melanoleuca*. The 14 aromatic amino acids mutated in this study are indicated as dark circles.

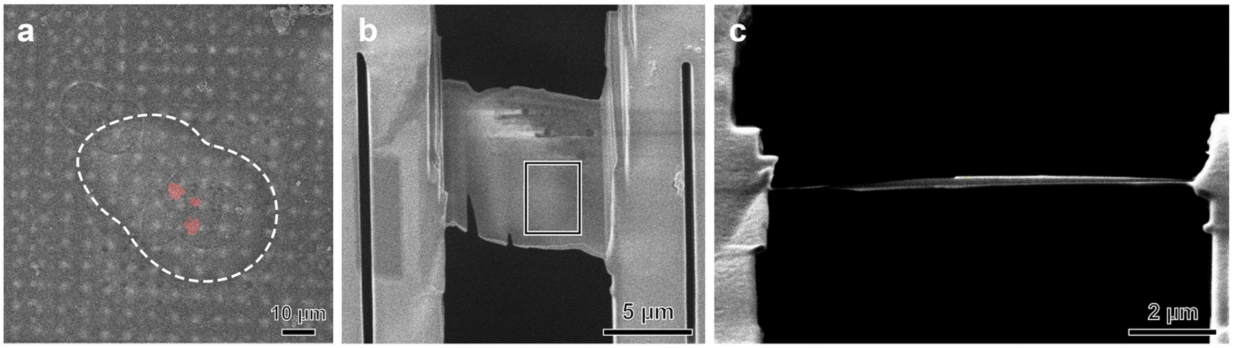

Supplementary Figure S9. Cryo-ET sample preparation of cells expressing RIBEYE_FL.

a SEM image of a frozen-hydrated HEK293T cell overlaid with a confocal fluorescence image of mCherry-tagged RIBEYE_FL. The mCherry signal guided subsequent cryo-FIB milling. The dashed line indicates the cell boundary.

b, c SEM view (**b**) and ion-beam view (**c**) of a ~150-nm-thick cryo-FIB-milled lamella. The boxed region was selected for high-magnification montage acquisition, with the resulting montage shown in Fig. 4g.

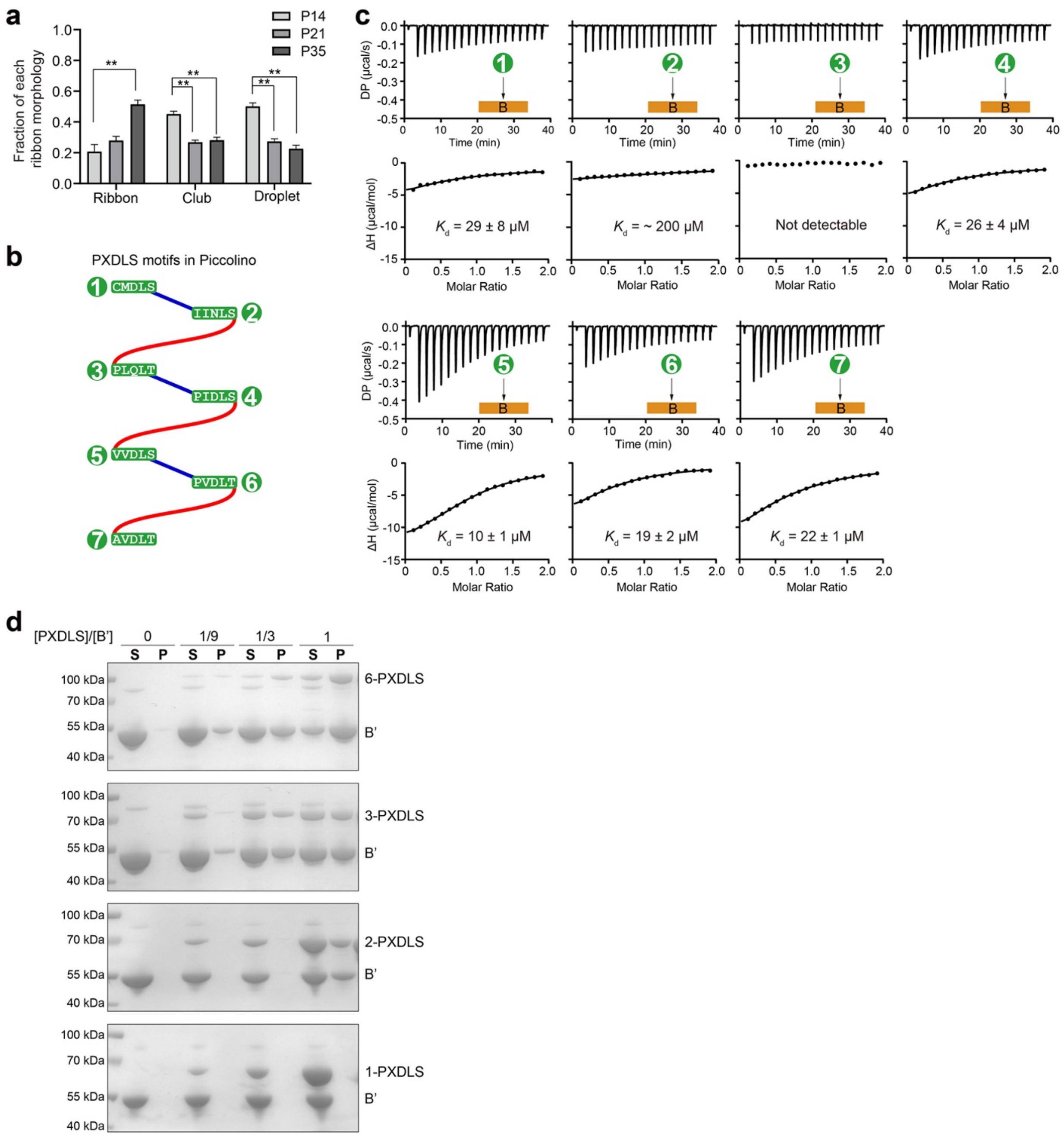

Supplementary Figure S10. The promotional effect of Piccolino on the RIBEYE-mediated ribbon formation.

a Quantification of the ribbon morphology shown in Fig. 5a. n = 4 animals. The estimate of variation is indicated by the s.e.m.. ANOVA followed by Tukey's multiple comparisons. **p < 0.01.

b Schematic diagram of the seven PXDLS motifs in the C-terminal region of Piccolino.

c ITC-based analysis of the binding of different PXDLS motifs to the B domain in RIBEYE.

d Raw SDS-PAGE data for quantification analysis shown in Fig. 5h.

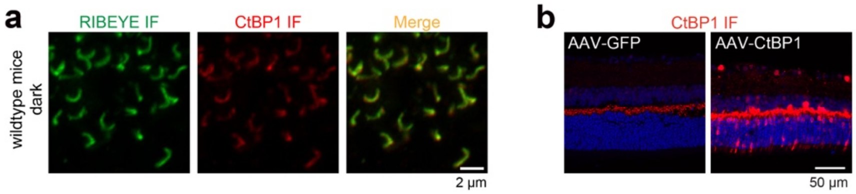

Supplementary Figure S11. The disruptive effect of CtBP1 on the RIBEYE-mediated ribbon formation.

a Representative images of the OPL from mice with dark adaptation. Sections were stained with CtBP1 (red) and RIBEYE (green) antibody.

b Representative images of the OPL from mice injected with AAV-EGFP or AAV-CtBP1. Sections were stained with CtBP1 antibody (red) and DAPI (blue).

Supplementary Video S1. Assembly modes of RIBEYE SAM domains in thick- and thin-filament forms.

Supplementary Video S2. Conformational transition between thick- and thin-filament forms of RIBEYE SAM domains.

Supplementary Video S3. Assembly mode of the B' filament via interactions between B tetramers and N-terminal extended linkers.

Supplementary Video S4. Cryotomogram and 3D rendering of B' sheets in a HeLa cell overexpressing RIBEYE_ΔIDR. This subvolume corresponds to the cryotomogram shown in Fig. 3a.

Supplementary Video S5. STA density map and fitted model of a single B' filament in the ribbon-like condensate of RIBEYE.

Supplementary Video S6. STA density map and fitted model of double B' filaments in the ribbon-like condensate of RIBEYE.

Supplementary Video S7. Cryotomogram and 3D rendering of perpendicularly oriented B' sheets in a HeLa cell overexpressing RIBEYE_ΔIDR. This subvolume corresponds to the cryotomogram shown in Fig. 3f.

Supplementary Video S8. Structure model of RIBEYE B' and SAM domains in mesoscale synaptic ribbon assembly. This model corresponds to the atomic model shown in Fig. 3g.

Supplementary Video S9. Cryotomogram and 3D rendering of B' sheets in a HEK293T cell overexpressing RIBEYE_FL. This subvolume corresponds to the cryotomogram shown in Fig. 4h.

Supplementary Table S1. The statistics of cryo-EM data collection, processing, model refinement, and validation.

Data collection and process	**SAM filament**		**B' filament**
Microscope	Titan Krios G3		Titan Krios G3i
Detector	Gatan K3		Gatan K3
Voltage(keV)	300		300
Total electron exposure (e- /Å^2)	50		50
Exposure time (s)	2.0		2.0
Electron exposure/frame (e- /Å^2)	1.56		1.56
Defocus range (μm)	-1.5 to -2.5		-1.5 to -2.5
Pixel size (Å)	0.415		0.46
Initial particle images (no.)	17495547		7756421
	Thick form	**Thin form**	
Final particle images (no.)	529850	57150	113042
Map resolution (Å)	3.37	3.39	3.41
FSC threshold	0.143	0.143	0.143
Map sharpening B factor (Å^2)	-158.2	-128.6	-51.7
Symmetry imposed	D1	D1	C1
Helical twist (°)	-35.953	-36.562	-157.078
Helical rise (Å)	17.000	21.066	55.737
Refinement			
Initial model used (PDB code)	AF2-predicted model	AF2-predicted model	6WKW
Model composition			
Non-hydrogen atoms	17816	14672	54720
Protein residues	2346	1932	6936
Ligands	0	0	20
R.M.S.D. from ideal geometry			
Bond lengths (Å)	0.004	0.005	0.003

Bond angles (°)	0.709	0.792	0.562
Validation			
CC_mask	0.73	0.77	0.75
Clashscore	10.61	15.56	4.61
MolProbity score	1.54	1.70	1.59
Poor rotamers (%)	0	0	0
Ramachandran plot statistics			
Favored (%)	98.51	100	94.83
Allowed (%)	1.49	0	5.17
Disallowed (%)	0	0	0